ACSNANO

www.acsnano.org

ARTICLE

Strong Room-Temperature Ferromagnetism in Ultrathin NiOOH Nanosheets through Surfactant Manipulation

Ziyi Zhang, Maciej P. Polak, Corey Carlos, Yutao Dong, Dane Morgan, and Xudong Wang*

Cite This: *ACS Nano* 2023, 17, 22979−22989

Read Online

ACCESS | Metrics & More | Article Recommendations | Supporting Information

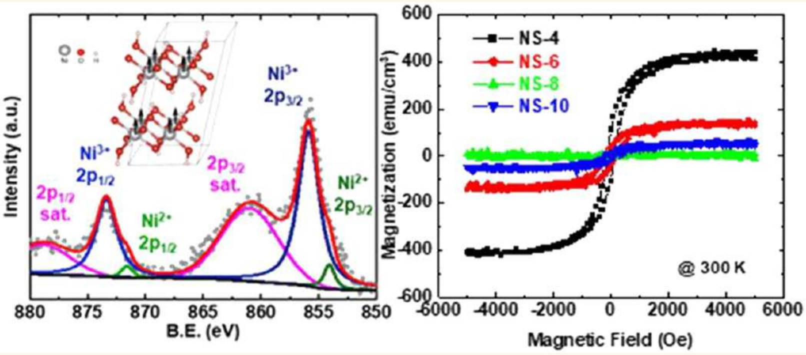

ABSTRACT: **Two-dimensional (2D) ferromagnetic (FM) materials with nanoscale thickness and spontaneous net magnetization have emerged as a promising class of functional materials for applications in next-generation spintronics, quantum processing, and data storage devices. However, most 2D materials exhibit weak FM even at low temperatures, limiting their potential applications in many technological fields. The fabrication of strong room-temperature FM 2D materials is highly desirable for the development of practical applications. Here, we demonstrate an ionic layer epitaxy strategy to synthesize few-layered NiOOH nanosheets with strong room-temperature FM and a saturation magnetization up to 409.86 emu cm^{-3} at 300 K. The results are consistent with the ab initio predictions of a stable FM NiOOH nanolayer structure with an FM configuration. The FM strength of the NiOOH nanosheets can be tuned by controlling the surfactant monolayer density and annealing. This work offers a promising strategy for achieving strong high-temperature FM in 2D materials for spintronic applications.**

KEYWORDS: *2D materials, ferromagnetism, ionic layer epitaxy, surface modification, defect engineering*

Ferromagnetic (FM) materials are a group of functional materials that exhibit spontaneous net magnetization below the Curie temperature. They have been widely studied in many research fields, including solid-state physics, materials science, and electronics.[1,2] Over the years, they have continuously attracted significant interest for their fascinating magnetic and spintronic properties for applications in modern electronics, such as information storage and logic devices.[3−5] As an emerging and impactful nanoscale material family, two-dimensional (2D) materials play significant roles in the development of new FM building blocks, which may set a cornerstone for next-generation quantum processing and memory devices.[6] For example, a long-range FM order was discovered in pristine $Cr_2Ge_2Te_6$ atomic layers,[7] while an out-of-plane FM spin orientation was observed in CrI_3 monolayers.[8] Following these exciting discoveries, there has been a fast growth in the prediction and investigation of a diverse range of 2D magnetic materials.[9−15]

However, intrinsic FM in most 2D materials has so far only been observed at low temperatures,[3] which largely limits their potential application in many technological fields. Exploring room-temperature 2D FM materials with tunable spin ordering is still essential. In addition to the anisotropic dimensionality effect,[7] strain[16,17] and impurities[18−21] can also tune the spin ordering, leading to FM. Although this enhancement is

Received: August 30, 2023
Revised: November 8, 2023
Accepted: November 9, 2023
Published: November 13, 2023

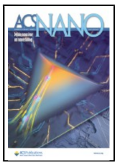

https://doi.org/10.1021/acsnano.3c08233

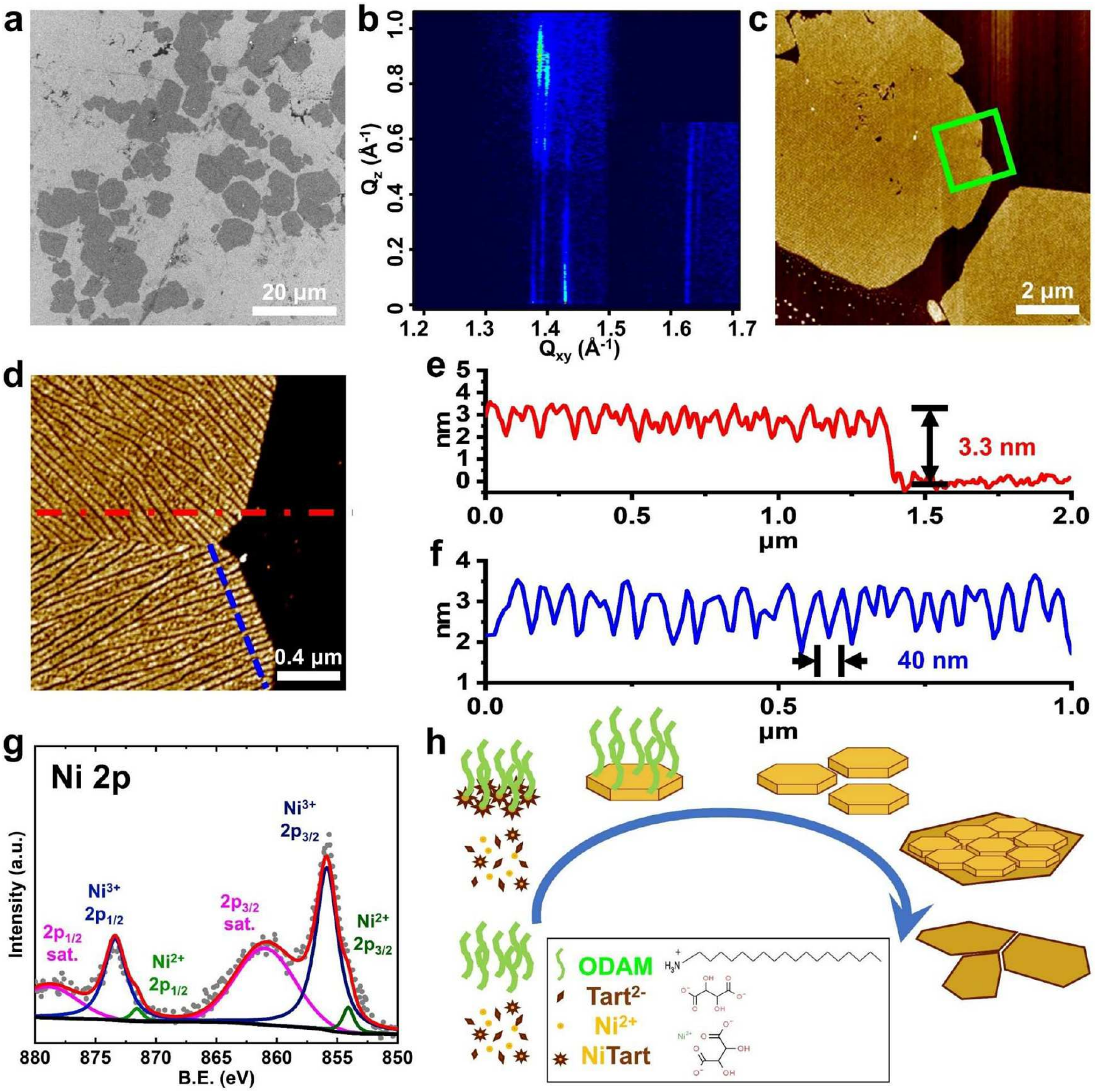

Figure 1. NiOOH NSs with unique surface features. (a) SEM image of the NiOOH NSs. (b) Grazing incidence X-ray diffraction data of the NiOOH NSs at the air−water interface. (c) AFM topography image of the NiOOH NSs. (d) Enlarged tiger-skin features from the green square area in (c). (e) Topographical line profile of the red dash-dot line in (d). (f) Topographical line profile of the blue dashed line in (d). (g) XPS Ni 2p spectrum. (h) Schematic illustration of the growth process of NiOOH NSs in the ILE synthesis.

generally weak in antiferromagnetic (antiFM) bulk phases, it can become particularly strong in 2D materials due to the significantly enhanced anisotropic electronic and magnetic structures in their ultrathin geometry.[22,23] NiOOH, a layered material which can be readily tuned by doping[24,25] and strain engineering,[26,27] may be able to be fabricated into a tunable FM 2D material. The 3d^7 Ni^{3+} oxidation state in NiOOH provides a large number of unpaired electrons in an ultrathin structure, which may lead to a strong magnetic moment. Although the experimental investigation of the magnetic properties of NiOOH has rarely been reported in the literature, bulk β-NiOOH was predicted as an FM material in an energy-favorable, low-spin configuration.[28] Theoretical predictions suggested that it may be possible to achieve a strong FM state in 2D NiOOH by manipulating its structure and introducing specific defects.[29,30]

Here, we demonstrate the strong room-temperature FM in NiOOH from a quasi-2D structure synthesized by ionic layer epitaxy (ILE).[31−33] The as-grown NiOOH nanosheet (NS) exhibited a saturation magnetization up to 409.86 emu cm^{-3} at 300 K. The magnetic properties of NiOOH NSs could be further tuned between FM and antiFM by controlling the surfactant density in the synthesis and annealing processes. A Ni valence state analysis and a density functional theory

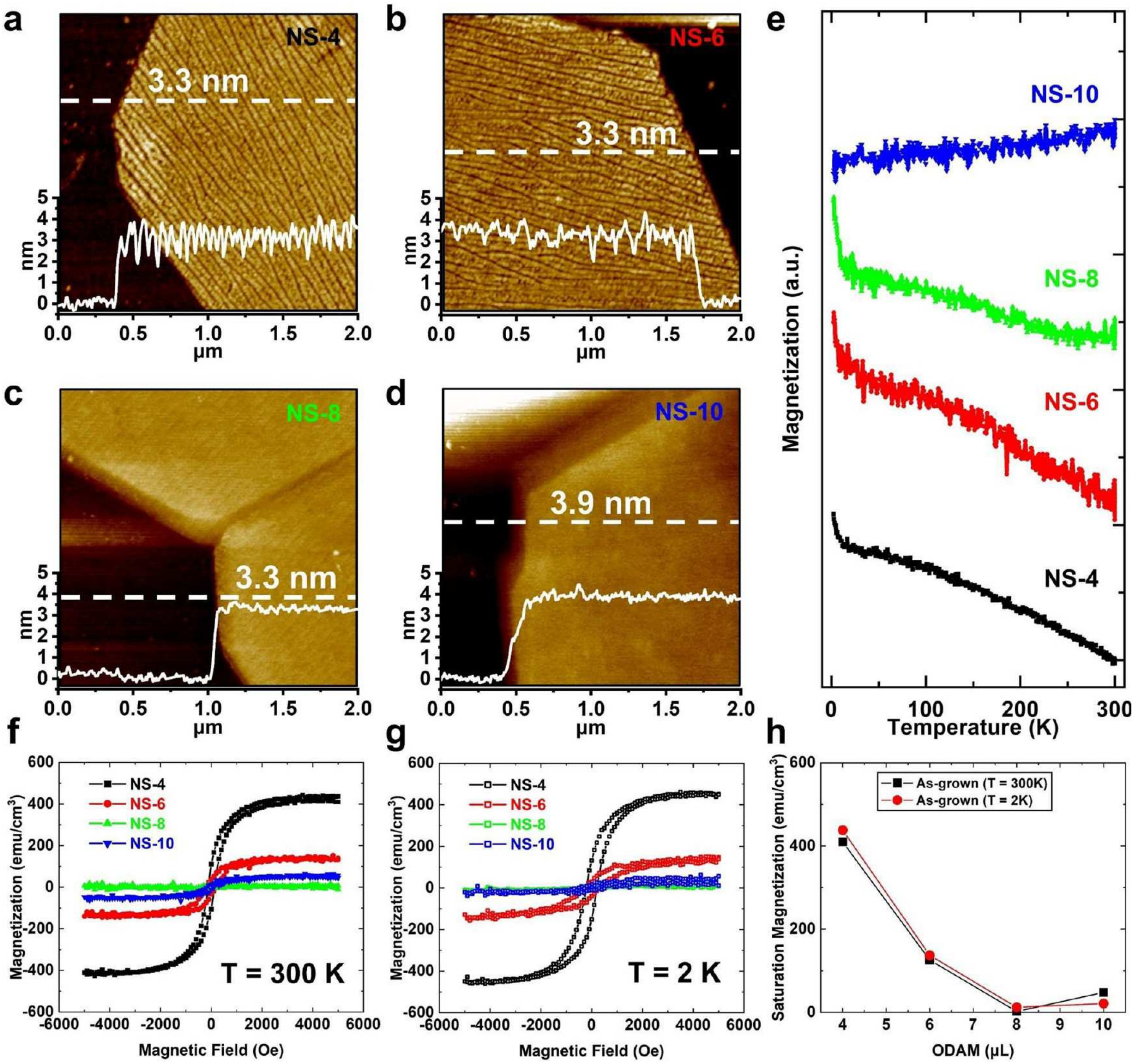

Figure 2. Ferromagnetic properties of the as-grown NiOOH NSs. AFM images of (a) NS-4, (b) NS-6, (c) NS-8, and (d) NS-10. (e) Temperature-dependent magnetizations with an applied field of 0.1 kOe. Hysteresis loops of NiOOH NSs at (f) 300 K and (g) 2 K. (h) Plot of the saturation magnetization of the NiOOH NSs vs the amount of ODAM employed.

(DFT) study suggested that the strong FM was associated with the Ni^{3+} component in the NSs. This study provides insights into the design and creation of 2D magnetic and spintronic materials with higher transition temperatures.

RESULTS AND DISCUSSION

2D NiOOH NSs were synthesized at the air−water interface through the ILE technique under the template of a monolayer of octadecylamine (ODAM) surfactant using $NiCl_2$ as the precursor (for details, see Methods). To avoid nucleation and particle growth in bulk solutions, ammonium tartrate (Tart) was added to coordinate and stabilize the Ni^{2+} ions.[34−36] Negatively charged Tart anions can also promote the accumulation of NiTart in the electrical double layer (EDL)[37] at the air−water interface, which facilitates the ODAM-directed NiOOH crystal nucleation and growth.[34] The spacing between the ODAM molecules increased after NiTart attached to the surfactant monolayer, as evidenced by the peak shifting from 1.499 to 1.428 $Å^{-1}$ in the liquid surface grazing incidence X-ray diffraction data (GIXD, Figure S1a,b).

The NiOOH NSs (NS-4, synthesized with 4 μL of ODAM) were collected from the water surface after 4 h of growth, and their morphology was characterized by scanning electron microscopy (SEM). A few micron-sized NSs merged into each other and formed large networks (Figure 1a). The lateral size of some of the larger pieces reached >500 μm (Figure S1c). The in-plane lattice structure of the NiOOH NSs at the air−water interface was studied in situ by GIXD during growth (Figure 1b). The diffraction rods at Q_{xy} = 1.376 and 1.624 $Å^{-1}$ could be assigned to the (100) and (110) planes of β-NiOOH with a $(3 \times 3)R30$ reconstruction.[38,39] The diffraction peak at 1.428 Å^{-1} was associated with the ODAM-assembled monolayer (Figure S1b). The intensities of the NS peaks were stronger in the high Q_z region, suggesting that the NSs grew under the ODAM monolayer at the interface. Moreover, the diffraction peak of the NSs located at 1.376 Å^{-1} on the left of that of ODAM (1.428 Å^{-1}) suggested that the NSs were grown under compressive strain from the ODAM monolayer. Next, the surface and thickness features of the NiOOH NSs were investigated by atomic force microscopy (AFM). The NSs possessed sharp hexagonal edge facets, which confirmed that the 2D crystal growth followed the closely packed surfactant molecule monolayer well at the water−air interface (Figure 1c). The entire as-grown NSs possessed a uniform thickness of 3.3 nm (Figure 1d,e). The high-magnification topography also resolved a periodic thickness fluctuation on the NS surface with a quasi-parallel pattern (Figure 1d). The average width of a single trench was ∼15 nm, and the spacing between the parallel trenches showed an average distance of 40 nm (Figure 1f). The X-ray photoelectron spectroscopy (XPS) Ni 2p spectrum of the NSs is presented in Figure 1g. The Ni $2p_{3/2}$ and $2p_{1/2}$ peaks did not show the typical multiplet-splits characteristic of a $NiO_x/Ni(OH)_2$ mixture.[30] The spectrum agreed with the results of $NiOOH/Ni(OH)_2$ peak fitting. This indicated that the NiOOH NS (Ni^{3+} $2p_{3/2}$, 855.9 eV) containing 7.4% Ni^{2+} was associated with the valence state of $Ni(OH)_2$ (Ni^{2+} $2p_{3/2}$, 854.1 eV). The amine head groups from the surfactant monolayer may have taken the hydrogen sites and allowed the NiOOH phase to be more favorable in the NSs than in typical bulk conditions. These characterizations also suggested that the NSs fabricated via ILE were few-layered NiOOH crystals and may contain a high concentration of defects due to the presence of Ni^{2+}.

The possible growth mechanism of the NiOOH NSs follows the typical ILE process and is schematically illustrated in Figure 1h. As the growth began, NiTarts were attracted by the ODAM monolayer and reached supersaturation in the EDL-confined region. According to the LaMer mechanism,[40] nanocrystal nucleation occurred at the air−water interface. Templated by the ODAM monolayer, the nuclei grew laterally into discrete micron-sized NiOOH NSs.[33] As the discrete NSs grew bigger, some of them contacted each other and merged.[31] During this process, the excess ODAM in the gap region between the NSs could have been compressed and trapped on the NS surface. The surface trenches were possibly created by the strain relaxation after the merging, while the ODAM may have spread out on the NS surface or filled the trenches to improve the uniform coverage over the NSs.

In previous kinetic studies of ILE growth dynamics,[33] it has been demonstrated that adjusting the surfactant packing density can tune the uniformity of the monolayer template and the charge density in the EDL, thus resulting in different NS assembly morphologies.[37] Here, the NiOOH NSs were also synthesized with different ODAM packing densities provided by 4, 6, 8, and 10 μL of ODAM. Accordingly, these NiOOH NSs were labeled NS-4, NS-6, NS-8, and NS-10, respectively. (It should be noted that due to the EDL-confined 2D crystal growth mechanism,[32,37] 4 μL of ODAM was the minimum amount of surfactant that was able to provide a well-assembled monolayer for uniform 2D crystalline NiOOH NSs growth (Figure S2). Additionally, because of the poor sample qualities of the NSs synthesized with lower ODAM amounts, their magnetic properties were not measured.) All of the samples followed the same structural evolution process. Compared to NS-4 and NS-6, the NSs grown under higher ODAM densities (NS-8 and NS-10) possessed a more merged morphology with a larger average grain size (Figure S3).[33,37] AFM topography scans revealed that NS-4, NS-6, and NS-8 were 3.3 nm in thickness, while NS-10 was 3.9 nm in thickness (Figure 2a−d). This greater thickness could be attributed to excessive ODAM molecules that may have formed a capping layer on the top surface of the NS (∼0.6 nm). Our previous electrochemical studies revealed that there was an ODAM capping layer on the as-grown NS surface. The more ODAM that was applied for NS growth, the thicker the capping layer that covered the crystalline NS surface became, resulting in an increased impedance for charge transfer across the NSs.[41] NS-4 and NS-6 exhibited a similar trench depth (d_t) of about 0.8 nm, while the trenches in NS-8 and NS-10 were largely diminished (d_t < 0.2 nm), yielding a smooth surface. This phenomenon indicates that excessive ODAM molecules were able to fill the gaps and eventually cap the entire surface.

The magnetic properties of the NiOOH NSs were characterized by a superconducting quantum interference device (SQUID). Because the ultrathin NiOOH NSs were flexible and stable under ambient conditions (Figure S1d, S4, and S5), all of the NSs were directly transferred from the solution surface onto sapphire substrates for the SQUID measurements. The magnetic properties of the bare sapphire substrate and pure ODAM, NiTart, and NiO powders were also measured as controls. It was determined that sapphire and ODAM were diamagnetic, NiTart was moderately paramagnetic, and the NiO powders were antiFM (Figures S6 and S7). None of them exhibited any FM behavior, which allowed us to obtain the FM properties of NiOOH NSs from the measurements. The as-grown NSs demonstrated obvious FM behaviors. Zero-field-cooled (ZFC) magnetizations were measured from 2 to 300 K with an in-plane magnetic field of 1 kOe (Figure S8). As the magnetization−temperature (M−T) curves show in Figure 2e, the magnetic properties of the as-grown NiOOH NSs varied among the samples made from different ODAM densities. The magnetic moments of both NS-4 and NS-6 showed an almost linear decreasing trend as the temperature increased, evidencing an obvious FM behavior. NS-8 exhibited a mixed temperature dependency, suggesting a weaker FM behavior at low temperatures, which then converted to antiFM above 270 K (Figure S8e). NS-10 was antiFM in the entire temperature range between 2 and 300 K according to the observed linear increasing trend with temperature. The M−H hysteresis curves of all four samples measured at 300 and 2 K are shown in panels f and g of Figure 2 (and panels a and b of Figure S9), respectively. Narrow "S-shaped" loops were observed at both temperatures, indicating the soft FM properties of these NiOOH NSs. NS-4 possessed the strongest saturation moments of 409.86 emu cm^{-3} at 300 K and 437.97 emu cm^{-3} at 2 K. The saturation magnetizations of these curves are summarized in Figure 2h and Table S1. The differences between the measurements at 300 and 2 K were consistent with the ZFC measurements. In general, a less dense ODAM monolayer promoted stronger FM in the as-grown NiOOH NSs. NS-10 possessed a slightly larger magnetization than NS-8, which may have been caused by a nonideal magnetic ordering in the defective structure induced by the nonuniform ODAM monolayer.[42] With higher ODAM coverage (e.g., 10 μL), the surfactant monolayer was more likely to form wrinkles and local islands rather than a perfect

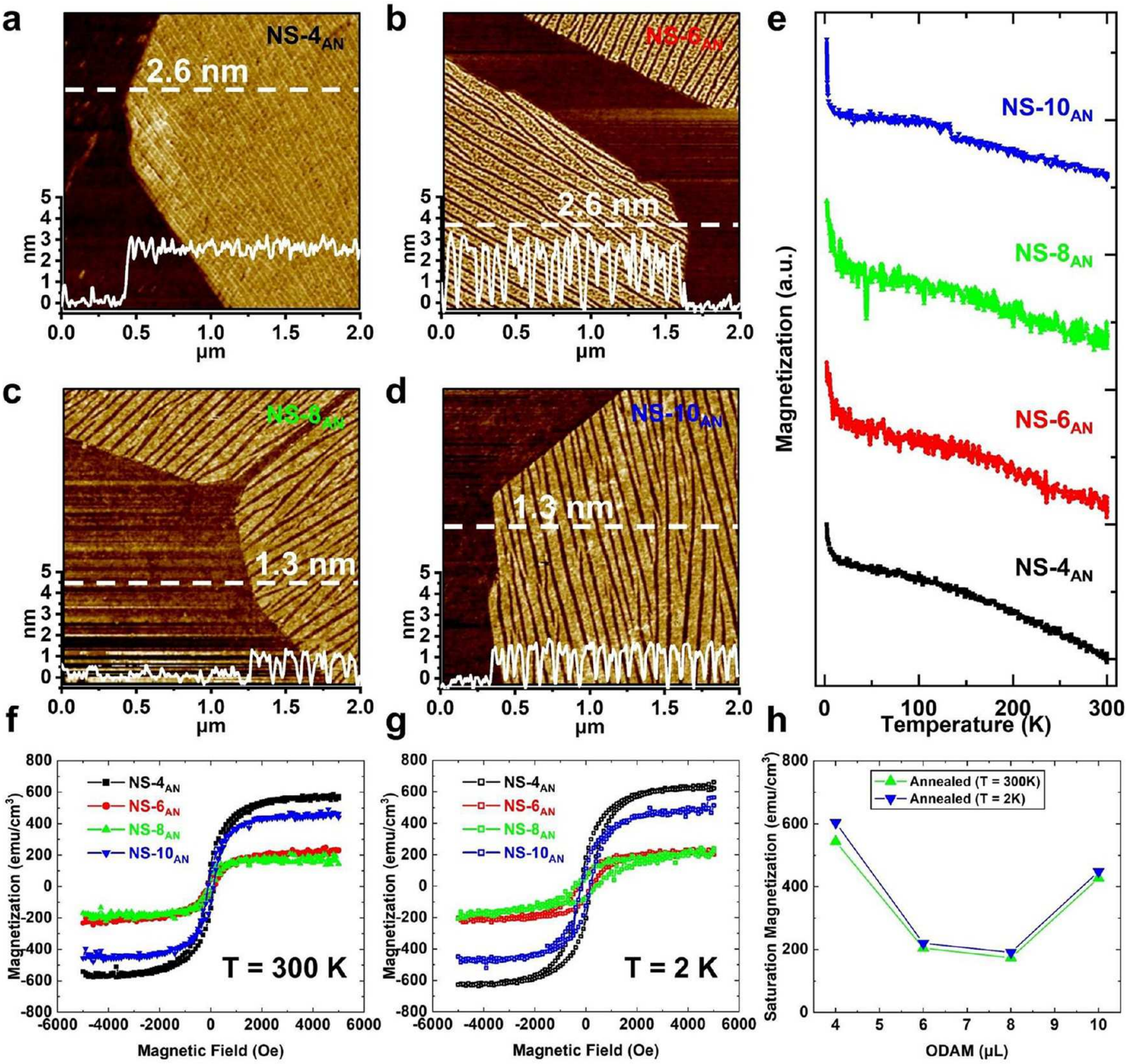

Figure 3. Ferromagnetic properties of NiOOH NSs after annealing 1 h in N_2 at 200 °C. AFM images of (a) NS-4, (b) NS-6, (c) NS-8, and (d) NS-10. (e) Temperature-dependent magnetizations with an applied field of 0.1 kOe. Hysteresis loops of NiOOH NSs at (f) 300 K and (g) 2 K. (h) Plot of the saturation magnetization of the NiOOH NSs vs the amount of ODAM employed.

flat structure. The weak S-shape behavior in the M−H curve of NS-10 at 300 K was possibly due to the thermal effects on the nonideal ordering of NS-10 and the ODAM capping on the surface. Additional M−H hysteresis and ZFC measurements were performed up to 400 K on the NS-4 and NS-10 samples (Figure S10). NS-4 maintained its FM behavior at 400 K. A magnetization maximum was observed at ∼348 K from the M−T curve of NS-10, showing a possible Neel temperature. These results further revealed how the magnetic properties of NiOOH NSs could be tuned by controlling the surfactant density.

To further confirm the influence of the surfactant and evaluate the magnetic properties of the NiOOH NSs, the four NS samples were annealed at 200 °C for 1 h with an N_2 flow of 40 sccm (standard cubic centimeters per minute) at a vacuum level of 800 mTorr to remove the surfactants. The structure and surface morphology of the annealed NiOOH NSs (NS-n_{AN}) were characterized by SEM (Figure S11) and AFM (Figure 3a−d). In all four samples, the hexagonal facets and the parallel trenches features were maintained without obvious reconstruction. The thickness line profiles shown in Figure 3a,b revealed a thickness reduction of 0.7 (to 2.6 nm) in NS-4_{AN} and NS-6_{AN}, indicating the successful removal of the surfactant. NS-8_{AN} and NS-10_{AN} were even thinner after annealing, only retaining a thickness of 1.3 nm, which is half that of NS-4_{AN} and NS-6_{AN} (Figure 3c,d). The smaller thicknesses of the NiOOH NSs were a result of the denser surfactant monolayer, which could build more charges at the air−water interface and promote the lateral growth of 2D crystals rather than thickness growth.[33] In addition, the

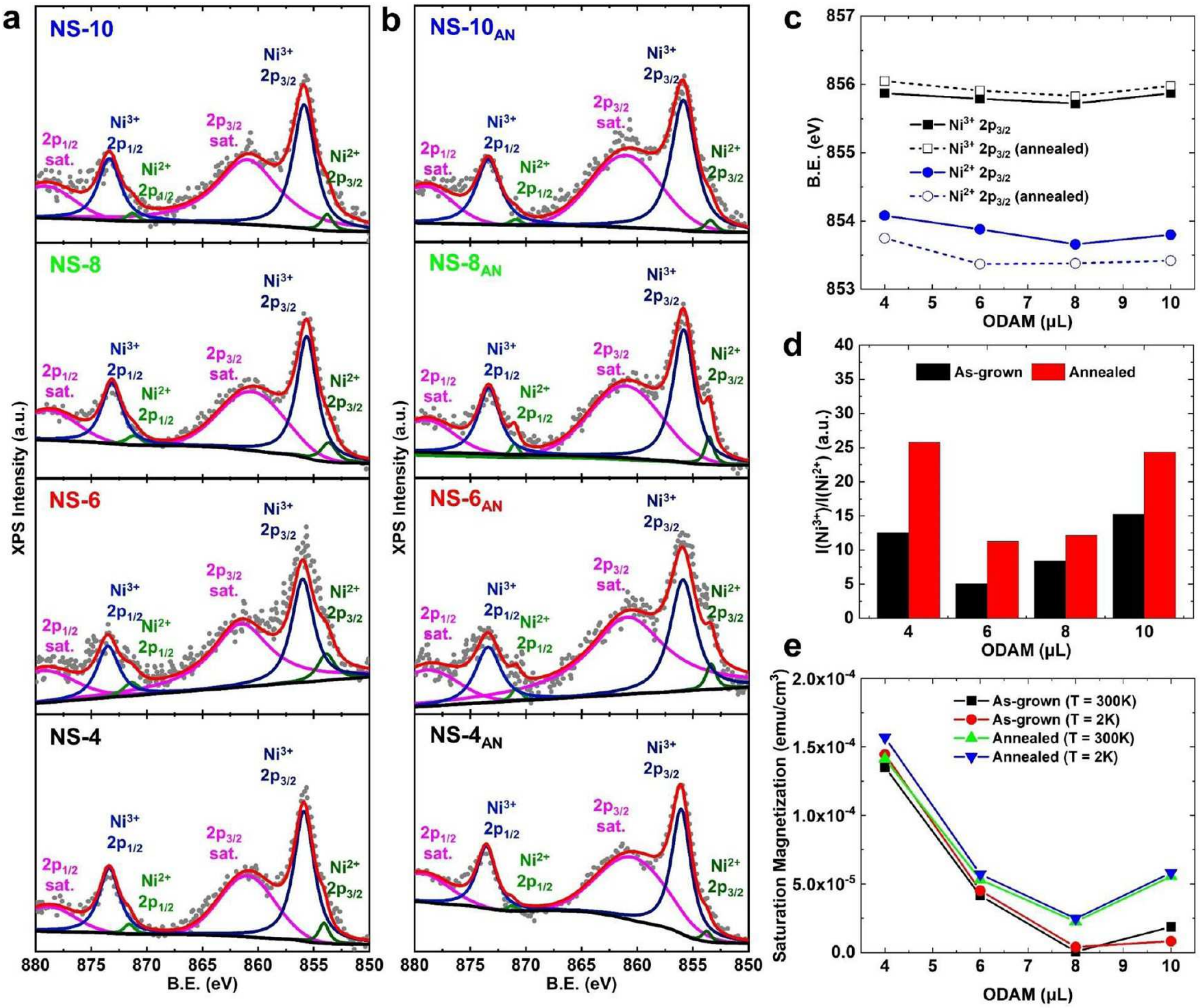

Figure 4. Surface properties and Ni valence states of the NiOOH NSs. XPS Ni 2p spectra of the (a) as-grown NSs and (b) annealed NSs. (c) XPS Ni 2p peak locations. (d) XPS intensity ratios of the Ni^{3+} and Ni^{2+} $2p_{3/2}$ peaks. (e) Saturation magnetization enhancement of the NiOOH NSs from annealing.

trenches became much deeper in the 6−10 μL samples, almost across the whole NS thickness. The greater thickness reduction that was observed in the NSs grown under denser ODAM suggested that there was a larger amount of surfactant capping on the as-grown NS surfaces.

The same set of magnetic property measurements was repeated for these four annealed samples. The M−T results presented in Figure 3e revealed that all of the annealed NiOOH NSs exhibited a typical FM temperature dependency from 2 to 300 K with a stronger FM behavior (Figure S8b). NS-8_{AN} and NS-10_{AN} were fully converted from antiFM to FM, showing a linear decreasing trend as the temperature increased. In the M−H curves, all four samples showed enhanced saturation moments compared to their pre-annealed counterparts, where NS-8_{AN} and NS-10_{AN} displayed distinct hysteresis S-shaped loops (Figures 3f,g and S9c,d). Moreover, NS-6_{AN} and NS-8_{AN} showed moderate magnetization, with their loops almost overlapping. NS-4_{AN} and NS-10_{AN} showed magnetizations that were stronger than those of the two samples with intermediate ODAM densities (Figure 3h). Similar FM was achieved in both the thick (2.6 nm, samples NS-4_{AN} and NS-6_{AN}) and thin (1.3 nm, samples NS-8_{AN} and NS-10_{AN}) NSs. Therefore, FM in NiOOH may not be directly related to the NS thickness.

The higher FM that was observed in the annealed NiOOH NSs may be due to the spin structure in the NS surface layer becoming more polarized when the capping surfactants were removed. In addition, the coercivities of NS-6_{AN} and NS-8_{AN} were higher than those of NS-4_{AN} and NS-10_{AN}. The harder FM indicated there was a larger magnetic domain size with longer-range ordering in the NSs. This could be related to the ordering of the surfactant monolayer during NS growth. The monolayers obtained from using 6 and 8 μL of ODAM were expected to possess a uniform packing that was closer to the lattice of the NiOOH (001) plane. Thus, the nanocrystals in the early growth stage were more likely to have rich epitaxial binding with the ODAM monolayer. The as-grown 2D NiOOH NSs yielded a higher crystallinity and large domain size, leading to harder magnets.[37] Because 4 μL of ODAM was not enough to fully cover the entire growth surface area, the

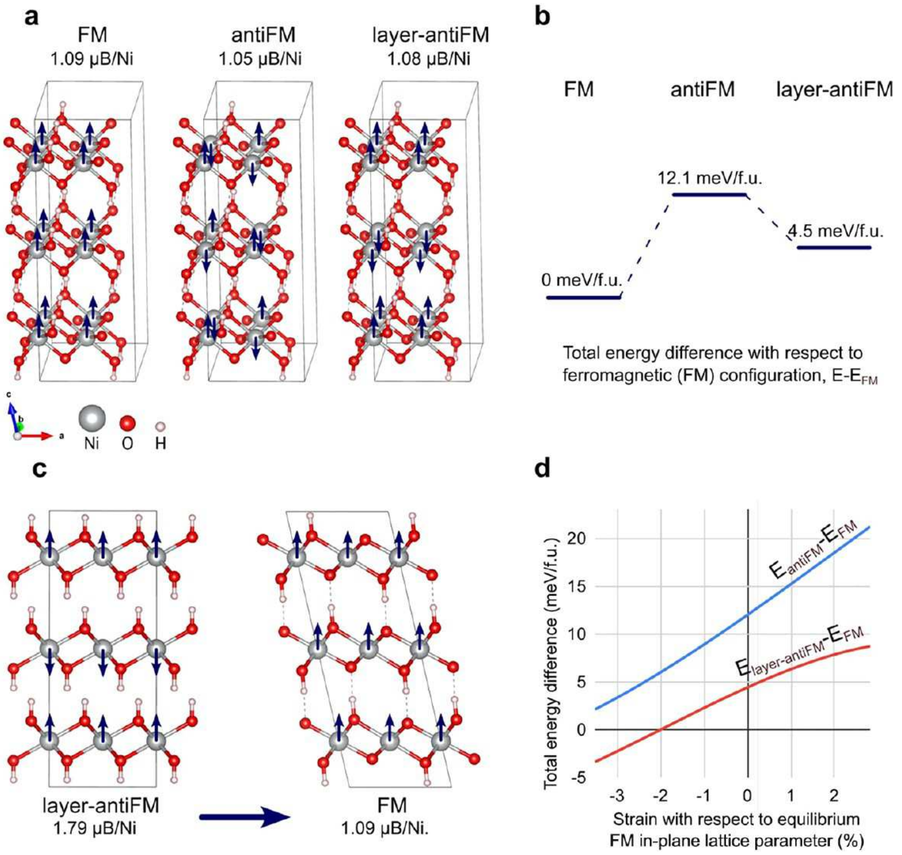

Figure 5. Summary of first-principles calculations for NSs. (a) Schematic of the considered magnetic spin configurations and their respective absolute values of magnetic moments per formula unit. (b) Total energy difference for the magnetic spin configurations presented in (a) with respect to the FM configuration. (c) Schematic showing the differences in the structures of antiFM $Ni(OH)_2$ and FM NiOOH. (d) Total energy difference between antiFM or layer-antiFM and FM as a function of strain with respect to the equilibrium FM configuration.

NSs were less likely to have large domain sizes with a higher possibility to form locally defective structures. In contrast, high ODAM concentrations (e.g., 10 μL) would lead to the formation of a wrinkled surfactant monolayer or multilayered islands. These features could have resulted in a higher concentration of defects or local disorders in the NiOOH NSs, which could have contributed to the enhanced FM property after annealing.[43]

To understand the antiFM-to-FM transition in the NiOOH NSs that occurred because of annealing and the subsequent removal of the surfactant, we analyzed the changes in the Ni oxidation state in all of the NSs using high-resolution XPS. Panels a and b of Figure 4 display the Ni 2p components of the NSs before and after annealing, respectively. It was found that all of the samples could be well-fit to a combination of Ni^{3+} and Ni^{2+} peaks. The binding energies of the Ni^{3+} $2p_{3/2}$ and Ni^{2+} $2p_{3/2}$ peaks were related to the amount of ODAM. Before annealing, the binding energy of the Ni^{3+} $2p_{3/2}$ peaks stayed at 855.9 eV, while the Ni^{2+} $2p_{3/2}$ peaks were red-shifted with the increase of ODAM (Figure 4c and Table S2). The N 1s spectra evidenced that ODAM was successfully removed from the NS surfaces after annealing (Figure S12). Because of the absence of ODAM, a moderate blue-shift of the Ni^{3+} $2p_{3/2}$ peaks (around +0.1 eV) and a red-shift of the Ni^{2+} $2p_{3/2}$ peaks were observed. The Ni^{2+} $2p_{3/2}$ peak for NS-4_{AN} was located at 853.7 eV, and that of the other three annealed samples were situated at ~853.4 eV. These Ni oxidation states revealed the charge transfer that occurred between Ni and amine (from ODAM) at the NS surface. Amine on the NS surface is a donor-type ligand[36] that reduces the oxidation state of the Ni^{3+} ions to the 2+ oxidation state.[44] Thus, when the ODAM molecules were removed from the NS surface, more Ni^{3+} was generated in the NiOOH structure. To evaluate the changes in the Ni valence state after annealing, the intensities of the Ni^{3+} $2p_{3/2}$ and Ni^{2+} $2p_{3/2}$ peaks of each sample were integrated and compared. The intensity ratio between the Ni^{3+} and Ni^{2+} $2p_{3/2}$ peaks ($I[Ni^{3+}]/I[Ni^{2+}]$) revealed the Ni valence difference in the NSs (Figure 4d and Table S3). An intensity ratio of 12.54 was found for NS-4, while that for NS-6 dropped to 5.06. The values for NS-8 and NS-10 were 8.42 and 15.22, respectively. After ODAM was removed by annealing, $I[Ni^{3+}]/I[Ni^{2+}]$ increased to 25.75, 11.23, 12.16, and 24.35 for NS-4_{AN}, NS-6_{AN}, NS-8_{AN}, and NS-10_{AN}, respectively. It was found that these ratios matched the saturation magnetization trend of the NSs. These results verified that the FM of the NSs was directly related to the Ni^{3+} component in the NiOOH NSs. The NS-4_{AN} and NS-10_{AN} samples, which had more Ni^{3+}, possessed a stronger FM compared to that of NS-6_{AN} and NS-8_{AN}, which had less Ni^{3+}. By engineering the thickness, defect concentration, and surface properties of the NSs, we obtained a a wide variety of magnetic 2D NiOOH NSs using the ILE technique (Figure 4e).

Because it is difficult to effectively and reliably control the defects and strain in the synthesis of NSs with atomic precision, it is extremely challenging to experimentally explore the origin of their magnetism by characterizing the defects and strain in such ultrathin 2D materials. Therefore, in order to better understand the structure and magnetism of NiOOH, we utilized ab initio methods (see Methods for technical details). We predicted the stable hydrogen locations and stable magnetic ordering for bulk NiOOH, as shown in Figure S13. These results suggest that NiOOH is a bulk ferromagnet (with the staggered-I structure; see the Supporting Information for details), which is consistent with previous studies. However, the energetic preference is just a few meV per formula unit (see Table S4), which leaves a possibility for a low-energy transition from FM to layer-antiFM.

A three-layer NiOOH (c = 4.86 Å) system was also studied respective to the 1.3 nm thick NSs, and similar to the bulk case, the staggered-I hydrogen structure with an FM configuration was found to be the ground state. Figure 5a,b shows the optimized staggered-I structure and the energy difference between the different magnetic configurations. The magnetic moments arising from the spin density difference in the FM NS are virtually identical to those predicted for bulk systems: 1.093 μB within a sphere of 1.286 Å centered on a Ni atom, and a total of 1 μB per formula unit, which results in effective magnetic moments (determined from the relationship described in the Methods section) of 1.732 and 1.893 μB; these values are in line with the expectation for Ni^{3+}. Previous calculations[28] have demonstrated that high-spin configurations are not stable. We confirmed this by initializing calculations from a higher magnetic moment of 4.5 μB, which always relaxed to a low-spin result. For comparison, the Ni^{2+} in $Ni(OH)_2$ has a magnetic moment with an average absolute value of ~1.79 μB at Ni with a total of 2 μB per formula unit, which results in effective magnetic moments of 2.531 and 2.828 μB for all magnetic configurations (Figure 5c). Similarly to NiOOH, reducing the bulk $Ni(OH)_2$ system to the NS does not change either the in-plane lattice parameters, magnetic moments, or magnetic configuration preference, which for $Ni(OH)_2$ is a layer-antiFM configuration (Figure 5c). This result suggests that the presence of excess hydrogen atoms, as suggested by the presence of Ni^{2+} in the XPS spectra, may locally induce a higher magnetic moment on the Ni atoms (characteristic of $Ni(OH)_2$) but keep the FM character due to the low energy difference of the transition from layer-antiFM to FM and the compressive strain from the surrounding NiOOH, thus effectively strengthening the FM of the NSs. In addition, the total energy with respect to in-plane strain was calculated. Figure 5d shows the energy preference expressed as the difference between the antiFM or layer-antiFM energies and the energy of the FM configuration. As can be seen from the plot, a compressive strain of ~2% with respect to the equilibrium FM in-plane lattice parameter is enough to switch the energy preference to layer-antiFM, which suggests that a moderate strain is capable of modulating the magnetic behavior and local strain. For example, a strain induced by epitaxial growth under the surfactant monolayer may be capable of locally inducing layer-antiFM behavior and lowering the effective magnetic moment. The combination of the local compressive strain induced by the surfactant, which is capable of lowering the effective magnetic moment, and small amounts of excessive hydrogen, which can locally change the oxidation state of Ni and increase its magnetic moment, can further tune the magnetic behavior of NiOOH NSs.

CONCLUSIONS

In summary, we synthesized a series of ultrathin NiOOH NSs at various ODAM surfactant densities via the ILE technique. Because of the ultrathin structure of the NSs, the NS thickness and Ni^{3+} concentration could be substantially modified by the density of the ODAM monolayer. The ground state FM configuration of NiOOH was stabilized by the epitaxial ODAM on the NS surface, resulting in a strong room-temperature FM. The as-grown NiOOH NS sample NS-4 reached a saturation magnetization of 409.86 emu cm^{-3} at 300 K. Further magnetic property studies revealed an FM-to-antiFM transition that was associated with an increasing surfactant density. XPS analyses and DFT calculations revealed that the FM of the NSs was suppressed by the electron doner-type capping of ODAM. Therefore, the FM of the NSs could be further enhanced by surfactant removal. With more Ni^{3+} being exposed in the annealed NSs, their saturation magnetizations were improved. It was also found that the magnetism of the NiOOH NSs could be further tuned by the strain induced by the surfactant monolayer. The insights obtained from this study offer a promising route toward the design and synthesis of 2D FM materials with extraordinarily strong room-temperature magnetization. Compared to rare-earth-element-based FM materials, earth-abundant Ni-based NSs can obtain superior magnetic properties from the facile and scalable ILE method, adding additional advantages to addressing environmental concerns in FM applications. Moreover, the FM NiOOH NSs may also show good electronic transport properties because of their nanoscale thickness and rich defects. With a further understanding of the charge transport and FM properties, the materials innovation from this work may eventually be utilized for developing next-generation memory and logic devices.

METHODS

Synthesis of NiOOH NSs. NiOOH NSs were synthesized by the ILE method. In a typical synthesis, a 10 mL aqueous solution containing 5 mM nickel(II) chloride ($NiCl_2$) and 4 mM ammonium tartrate (Tart) was prepared in a 20 mL glass vial (with an inner diameter of 24 mm) by subsequently dissolving ammonium L-tartrate (Sigma-Aldrich) and $NiCl_2·6H_2O$ (Sigma-Aldrich) powders. Then, a small droplet of a chloroform solution containing 1.8 mM octadecylamine (ODAM, Sigma-Aldrich) was slowly added to the surface of the precursor solution (e.g., 4 μL of ODAM formed a self-assembled monolayer with a density of 0.096 ODAM $Å^{-2}$). Finally, the glass vial was kept at ambient conditions for 4 h. The NiOOH NSs could be transferred onto an arbitrary substrate by scooping at the surface of the solution or extracting the solution from the bottom of the vial for characterization and device fabrication. The NiOOH NSs were transferred on double-sided polished single-crystalline sapphire substrates (5 × 5 × 0.5 mm, AdValue Technology) for magnetic property characterizations. Si substrates were used for the other NS characterizations.

NiOOH NS Characterizations. A Zeiss LEO 1530 field-emission scanning electron microscope (FESEM) was used to study the morphologies of the NiOOH NSs. Atomic force microscopy (AFM) tomography images were obtained by using an XE-70 Park Ssystems instrument. X-ray photoelectron spectroscopy (XPS) was performed on a Thermo Scientific K-Alpha XPS instrument using a spot size of 400 μm and with the flood gun turned on during the measurements. In situ grazing incidence X-ray diffraction (GXID) experiments were performed at beamline 15-ID-C ChemMatCARS at the Advanced Photon Source (APS) in the Argonne National Laboratory. A 100 mL precursor solution was prepared in a Teflon trough with a 60 cm^2 open area (6 cm × 10 cm), and 53.5 μL of a ODAM solution was added to the surface to achieve the same surfactant density as with the growth using 4 μL of ODAM in the 20 mL glass vial.

Magnetic Property Measurements. A superconducting quantum interference device (SQUID, Quantum Design MPMS3 EverCool) with a magnetometer in direct current (DC) mode was used for all of the magnetic property measurements for the NiOOH NSs. M−H hysteresis loops ranging from −5000 to +5000 Oe were measured with an applied magnetic field parallel to the substrate at temperatures of 300 and 2 K. ZFC M−T curves were measured at 1000 Oe from 2 to 300 K. The obtained results of NiOOH NSs were processed by subtracting the diamagnetism of the sapphire substrate.

DFT Calculations. The Vienna Ab Initio Simulation Package (VASP) was used for the density functional theory (DFT) calculations in this study.[45,46] The energy cutoff for the plane wave basis set was set to 600 eV. For each calculation, the ions were allowed to relax using the conjugate-gradient algorithm until the maximum force in the system did not exceed 0.01 eV A^{-1}, while the convergence of each self-consistent field (SCF) cycle was set to 1×10^{-5} eV/atom. A 10 × 10 × 8 Γ-centered *k*-point mesh for a primitive unit cell equivalent was used, which resulted in a 5 × 5 × 4 mesh for the 2 × 2 × 2 supercell and a 5 × 5 × 1 mesh for the thin layers constructed from a 2 × 2 × 8 supercell. The on-site Coulomb interactions were treated within Dudarev's approach to DFT+U[47] with a U-J value of 5.5 eV on the Ni atoms, as suggested by previous research through linear response theory.[48] Spin polarization was included in all calculations. First, we determined the different atomic arrangements of the hydrogen atoms using a 2 × 2 × 2 supercell, which allowed us to consistently study the most likely low-energy configurations. An equal-sized 2 × 2 × 2 supercell was used to study the different magnetic configurations. The effective magnetic moment was calculated from the magnetic moments arising from the difference in the spin up and spin down charge (μ) according to the formula $\mu_{\text{eff}} = \sqrt{\mu(\mu+2)}$. For modeling the NSs, a three-monolayer system was initially built from optimized bulk structures by constructing a 2 × 2 × 8 supercell and removing 5 of the 8 layers, which resulted in 3 layers of NiOOH and a vacuum of around 26 Å (the equivalent thickness to that of the 5 removed layers). The in-plane lattice constant was then varied by ±3% in intervals of 0.5%, allowing the atoms to fully optimize their positions each time, and a third-order polynomial was fit to the converged energies to determine the minimum energy and final lattice parameters, which in all cases ended up being virtually the same as those for the bulk systems. Table S5 shows all of the optimized in-plane lattice constants, the NS thicknesses, the total energy differences with respect to the ground state FM, and a summary of the calculated magnetic moments.

ASSOCIATED CONTENT

Supporting Information

The Supporting Information is available free of charge at https://pubs.acs.org/doi/10.1021/acsnano.3c08233.

Additional $Ni(OH)_2$ NS characterizations, including SEM and GIXD images and magnetic property characterizations (PDF)

AUTHOR INFORMATION

Corresponding Author

Xudong Wang − *Department of Materials Science and Engineering, University of Wisconsin−Madison, Madison, Wisconsin 53706, United States;* orcid.org/0000-0002-9762-6792; Email: xudong.wang@wisc.edu

Authors

Ziyi Zhang − *Department of Materials Science and Engineering, University of Wisconsin−Madison, Madison, Wisconsin 53706, United States;* orcid.org/0000-0001-9102-8292

Maciej P. Polak − *Department of Materials Science and Engineering, University of Wisconsin−Madison, Madison, Wisconsin 53706, United States;* orcid.org/0000-0001-7198-7779

Corey Carlos − *Department of Materials Science and Engineering, University of Wisconsin−Madison, Madison, Wisconsin 53706, United States;* orcid.org/0000-0002-9398-2554

Yutao Dong − *Department of Materials Science and Engineering, University of Wisconsin−Madison, Madison, Wisconsin 53706, United States;* orcid.org/0000-0003-3582-087X

Dane Morgan − *Department of Materials Science and Engineering, University of Wisconsin−Madison, Madison, Wisconsin 53706, United States;* orcid.org/0000-0002-4911-0046

Complete contact information is available at: https://pubs.acs.org/10.1021/acsnano.3c08233

Author Contributions

Z.Z. developed the ILE method and synthesized all of the NS samples. Z.Z. carried out the SEM, XPS, and SQUID characterizations. C.C. and Z.Z. obtained the AFM measurements. Z.Z., C.C., and Y.D. conducted the in situ X-ray experiments at APS, Argonne National Lab. M.P.P. calculated the theoretical simulations. Z.Z. organized all of the data and wrote the manuscript. D.M. and X.W. supervised the project. All authors discussed the results, revised the manuscript, and gave approval for the final version of this manuscript.

Notes

The authors declare no competing financial interest.

ACKNOWLEDGMENTS

This work was primarily supported by the National Science Foundation DMR-2114931. The GIXD data were collected at NSF's ChemMatCARS Sector 15, which was principally supported by the Divisions of Chemistry (CHE) and Materials Research (DMR) of the National Science Foundation under Grant NSF/CHE-1834750. The use of the Advanced Photon Source, an Office of Science User Facility operated for the U.S. Department of Energy (DOE) Office of Science by Argonne National Laboratory, was supported by the U.S. DOE under Contract DE-AC02-06CH11357.

REFERENCES

(1) Dietl, T. Ferromagnetic semiconductors. *Semicond. Sci. Technol.* **2002**, *17* (4), 377.

(2) Tanaka, M. Recent progress in ferromagnetic semiconductors and spintronics devices. *Jpn. J. Appl. Phys.* **2021**, *60* (1), 010101.

(3) Zhao, Z.; Li, W.; Zeng, Y.; Huang, X.; Yun, C.; Zhang, B.; Hou, Y. Structure engineering of 2D materials toward magnetism modulation. *Small Structures* **2021**, *2* (10), 2100077.

(4) Fert, A. Nobel Lecture: Origin, development, and future of spintronics. *Reviews of modern physics* **2008**, *80* (4), 1517.

(5) Hirohata, A.; Yamada, K.; Nakatani, Y.; Prejbeanu, I.-L.; Diény, B.; Pirro, P.; Hillebrands, B. Review on spintronics: Principles and device applications. *J. Magn. Magn. Mater.* **2020**, *509*, 166711.

(6) Huang, C.; Feng, J.; Wu, F.; Ahmed, D.; Huang, B.; Xiang, H.; Deng, K.; Kan, E. Toward Intrinsic Room-Temperature Ferromagnetism in Two-Dimensional Semiconductors. *J. Am. Chem. Soc.* **2018**, *140* (36), 11519−11525.

(7) Gong, C.; Li, L.; Li, Z.; Ji, H.; Stern, A.; Xia, Y.; Cao, T.; Bao, W.; Wang, C.; Wang, Y.; Qiu, Z. Q.; Cava, R. J.; Louie, S. G.; Xia, J.; Zhang, X. Discovery of intrinsic ferromagnetism in two-dimensional van der Waals crystals. *Nature* **2017**, *546* (7657), 265−269.

(8) Huang, B.; Clark, G.; Navarro-Moratalla, E.; Klein, D. R.; Cheng, R.; Seyler, K. L.; Zhong, D.; Schmidgall, E.; McGuire, M. A.; Cobden, D. H.; Yao, W.; Xiao, D.; Jarillo-Herrero, P.; Xu, X. Layer-dependent

ferromagnetism in a van der Waals crystal down to the monolayer limit. *Nature* **2017**, *546* (7657), 270−273.

(9) Bonilla, M.; Kolekar, S.; Ma, Y.; Diaz, H. C.; Kalappattil, V.; Das, R.; Eggers, T.; Gutierrez, H. R.; Phan, M.-H.; Batzill, M. Strong room-temperature ferromagnetism in VSe2 monolayers on van der Waals substrates. *Nature Nanotechnol.* **2018**, *13* (4), 289−293.

(10) Chen, C.; Chen, X.; Wu, C.; Wang, X.; Ping, Y.; Wei, X.; Zhou, X.; Lu, J.; Zhu, L.; Zhou, J.; Zhai, T.; Han, J.; Xu, H. Air-Stable 2D Cr $_5$ Te $_8$ Nanosheets with Thickness-Tunable Ferromagnetism. *Adv. Mater.* **2022**, *34* (2), 2107512.

(11) Kim, H. H.; Yang, B.; Li, S.; Jiang, S.; Jin, C.; Tao, Z.; Nichols, G.; Sfigakis, F.; Zhong, S.; Li, C.; Tian, S.; Cory, D. G.; Miao, G.-X.; Shan, J.; Mak, K. F.; Lei, H.; Sun, K.; Zhao, L.; Tsen, A. W. Evolution of interlayer and intralayer magnetism in three atomically thin chromium trihalides. *Proc. Natl. Acad. Sci. U. S. A.* **2019**, *116* (23), 11131−11136.

(12) O'Hara, D. J.; Zhu, T.; Trout, A. H.; Ahmed, A. S.; Luo, Y. K.; Lee, C. H.; Brenner, M. R.; Rajan, S.; Gupta, J. A.; McComb, D. W.; Kawakami, R. K. Room temperature intrinsic ferromagnetism in epitaxial manganese selenide films in the monolayer limit. *Nano Lett.* **2018**, *18* (5), 3125−3131.

(13) Wang, X.; Li, D.; Li, Z.; Wu, C.; Che, C.-M.; Chen, G.; Cui, X. Ferromagnetism in 2D Vanadium Diselenide. *ACS Nano* **2021**, *15* (10), 16236−16241.

(14) Wu, H.; Zhang, W.; Yang, L.; Wang, J.; Li, J.; Li, L.; Gao, Y.; Zhang, L.; Du, J.; Shu, H.; Chang, H. Strong intrinsic room-temperature ferromagnetism in freestanding non-van der Waals ultrathin 2D crystals. *Nat. Commun.* **2021**, *12* (1), 5688.

(15) Zhang, G.; Guo, F.; Wu, H.; Wen, X.; Yang, L.; Jin, W.; Zhang, W.; Chang, H. Above-room-temperature strong intrinsic ferromagnetism in 2D van der Waals Fe3GaTe2 with large perpendicular magnetic anisotropy. *Nat. Commun.* **2022**, *13* (1), 5067.

(16) Pu, M.; Guo, Y.; Guo, W. Strain-mediated oxygen evolution reaction on magnetic two-dimensional monolayers. *Nanoscale Horizons* **2022**, *7* (11), 1404−1410.

(17) Wang, L.; Zhou, G.; Shan, Y.; Huang, Z.; Liu, L. Oxygen-defect-dependent ferromagnetism and strain modulation in free-standing two-dimensional TiO 2 monolayers. *Phys. Chem. Chem. Phys.* **2018**, *20* (42), 27176−27184.

(18) Du, L.; Gao, B.; Xu, S.; Xu, Q. Strong ferromagnetism of g-C3N4 achieved by atomic manipulation. *Nat. Commun.* **2023**, *14* (1), 2278.

(19) Husremović, S.; Groschner, C. K.; Inzani, K.; Craig, I. M.; Bustillo, K. C.; Ercius, P.; Kazmierczak, N. P.; Syndikus, J.; Van Winkle, M.; Aloni, S.; Taniguchi, T.; Watanabe, K.; Griffin, S. M.; Bediako, D. K. Hard ferromagnetism down to the thinnest limit of iron-intercalated tantalum disulfide. *J. Am. Chem. Soc.* **2022**, *144* (27), 12167−12176.

(20) Wei, N.; He, L.; Wu, C.; Lu, D.; Li, R.; Shi, H.; Lan, H.; Wen, Y.; He, J.; Long, Y.; Wang, X.; Zeng, M.; Fu, L. Room-Temperature Magnetism in 2D $MnGa_4$-H Induced by Hydrogen Insertion. *Adv. Mater.* **2023**, *35* (20), 2210828.

(21) Chen, R.; Luo, F.; Liu, Y.; Song, Y.; Dong, Y.; Wu, S.; Cao, J.; Yang, F.; N'Diaye, A.; Shafer, P.; Liu, Y.; Lou, S.; Huang, J.; Chen, X.; Fang, Z.; Wang, Q.; Jin, D.; Cheng, R.; Yuan, H.; Birgeneau, R. J.; Yao, J. Tunable room-temperature ferromagnetism in Co-doped two-dimensional van der Waals ZnO. *Nat. Commun.* **2021**, *12* (1), 3952.

(22) Sakamoto, Y.; Noda, Y.; Ohno, K.; Koike, K.; Fujii, K.; Suzuki, T. M.; Morikawa, T.; Nakamura, S. First principles calculations of surface dependent electronic structures: a study on β-FeOOH and γ-FeOOH. *Phys. Chem. Chem. Phys.* **2019**, *21* (34), 18486−18494.

(23) Tang, Z.-K.; Liu, W.-W.; Zhang, D.-Y.; Lau, W.-M.; Liu, L.-M. Tunable band gap and magnetism of the two-dimensional nickel hydroxide. *RSC Adv.* **2015**, *5* (94), 77154−77158.

(24) Hamal, E. K.; Toroker, M. C. The Effect of Fe and Co Additions on the Efficiency of NiOOH Catalyst Under Strain. *ChemCatChem.* **2020**, *12* (10), 2801−2806.

(25) Rathore, D.; Banerjee, A.; Pande, S. Bifunctional tungsten-doped Ni (OH) 2/NiOOH nanosheets for overall water splitting in an alkaline medium. *ACS Applied Nano Materials* **2022**, *5* (2), 2664−2677.

(26) Zhou, Z.; Xie, Y.-n.; Sun, L.; Wang, Z.; Wang, W.; Jiang, L.; Tao, X.; Li, L.; Li, X.-H.; Zhao, G. Strain-induced in situ formation of NiOOH species on CoCo bond for selective electrooxidation of 5-hydroxymethylfurfural and efficient hydrogen production. *Applied Catalysis B: Environmental* **2022**, *305*, 121072.

(27) Kuai, C.; Zhang, Y.; Han, L.; Xin, H. L.; Sun, C.-J.; Nordlund, D.; Qiao, S.; Du, X.-W.; Lin, F. Creating compressive stress at the NiOOH/NiO interface for water oxidation. *Journal of Materials Chemistry A* **2020**, *8* (21), 10747−10754.

(28) Tkalych, A. J.; Yu, K.; Carter, E. A. Structural and electronic features of β-Ni (OH) 2 and β-NiOOH from first principles. *J. Phys. Chem. C* **2015**, *119* (43), 24315−24322.

(29) Li, Y.-F.; Li, J.-L.; Liu, Z.-P. Structure and catalysis of NiOOH: Recent advances on atomic simulation. *J. Phys. Chem. C* **2021**, *125* (49), 27033−27045.

(30) Van der Ven, A.; Morgan, D.; Meng, Y.; Ceder, G. Phase stability of nickel hydroxides and oxyhydroxides. *J. Electrochem. Soc.* **2006**, *153* (2), A210.

(31) Wang, F.; Seo, J.-H.; Luo, G.; Starr, M. B.; Li, Z.; Geng, D.; Yin, X.; Wang, S.; Fraser, D. G.; Morgan, D.; Ma, Z.; Wang, X. Nanometre-thick single-crystalline nanosheets grown at the water−air interface. *Nat. Commun.* **2016**, *7* (1), 10444.

(32) Wang, Y.; Shi, Y.; Zhang, Z.; Carlos, C.; Zhang, C.; Bhawnani, K.; Li, J.; Wang, J.; Voyles, P. M.; Szlufarska, I.; Wan, X. Bioinspired synthesis of quasi-two-dimensional monocrystalline oxides. *Chem. Mater.* **2019**, *31* (21), 9040−9048.

(33) Zhang, Z.; Carlos, C.; Wang, Y.; Dong, Y.; Yin, X.; German, L.; Berg, K. J.; Bu, W.; Wang, X. Nucleation Kinetics and Structure Evolution of Quasi-Two-Dimensional ZnO at the Air−Water Interface: An In Situ Time-Resolved Grazing Incidence X-ray Scattering Study. *Nano Lett.* **2022**, *22* (7), 3040−3046.

(34) Janusz, W.; Skwarek, E. Comparison of oxalate, citrate and tartrate ions adsorption in the hydroxyapatite/aqueous electrolyte solution system. *Colloids and Interfaces* **2020**, *4* (4), 45.

(35) Neveu, S.; Bee, A.; Robineau, M.; Talbot, D. Size-selective chemical synthesis of tartrate stabilized cobalt ferrite ionic magnetic fluid. *J. Colloid Interface Sci.* **2002**, *255* (2), 293−298.

(36) Owen, J. The coordination chemistry of nanocrystal surfaces. *Science* **2015**, *347* (6222), 615−616.

(37) Yin, X.; Shi, Y.; Wei, Y.; Joo, Y.; Gopalan, P.; Szlufarska, I.; Wang, X. Unit Cell Level Thickness Control of Single-Crystalline Zinc Oxide Nanosheets Enabled by Electrical Double-Layer Confinement. *Langmuir* **2017**, *33* (31), 7708−7714.

(38) Cappus, D.; Haßel, M.; Neuhaus, E.; Heber, M.; Rohr, F.; Freund, H.-J. Polar surfaces of oxides: reactivity and reconstruction. *Surf. Sci.* **1995**, *337* (3), 268−277.

(39) Zhang, H.; May, B. M.; Serrano-Sevillano, J.; Casas-Cabanas, M.; Cabana, J.; Wang, C.; Zhou, G. Facet-dependent rock-salt reconstruction on the surface of layered oxide cathodes. *Chem. Mater.* **2018**, *30* (3), 692−699.

(40) De Yoreo, J. J.; Vekilov, P. G. Principles of crystal nucleation and growth. *Reviews in mineralogy and geochemistry* **2003**, *54* (1), 57−93.

(41) Zhang, Z.; Dong, Y.; Carlos, C.; Wang, X. Surface Ligand Modification on Ultrathin Ni(OH) $_2$ Nanosheets Enabling Enhanced Alkaline Ethanol Oxidation Kinetics. *ACS Nano* **2023**, *17* (17), 17180−17189.

(42) Koçer, C. P.; Griffith, K. J.; Grey, C. P.; Morris, A. J. First-principles study of localized and delocalized electronic states in crystallographic shear phases of niobium oxide. *Phys. Rev. B* **2019**, *99* (7), 075151.

(43) Kaminski, A.; Das Sarma, S. Polaron percolation in diluted magnetic semiconductors. *Phys. Rev. Lett.* **2002**, *88* (24), 247202.

(44) Guerrero-Ortega, L.; Ramírez-Meneses, E.; Betancourt, I.; Lartundo-Rojas, L.; Mendoza-Cruz, R.; Torres-Huerta, A.; Domínguez-Crespo, M. Effect of Alkyl Chain Length of Amines on the Micro-structural and Magnetic Properties of Stabilized Ni-NiO

Nanoparticles. *Journal of Inorganic and Organometallic Polymers and Materials* **2023**, *33* (2), 368−382.

(45) Hohenberg, P.; Kohn, W. Inhomogeneous Electron Gas. *Phys. Rev.* **1964**, *136* (3B), B864−B871.

(46) Kohn, W.; Sham, L. J. Self-Consistent Equations Including Exchange and Correlation Effects. *Phys. Rev.* **1965**, *140* (4A), A1133−A1138.

(47) Dudarev, S. L.; Botton, G. A.; Savrasov, S. Y.; Humphreys, C. J.; Sutton, A. P. Electron-energy-loss spectra and the structural stability of nickel oxide: An LSDA+U study. *Phys. Rev. B* **1998**, *57* (3), 1505−1509.

(48) Li, Y.-F.; Selloni, A. Mechanism and Activity of Water Oxidation on Selected Surfaces of Pure and Fe-Doped NiOx. *ACS Catal.* **2014**, *4* (4), 1148−1153.

https://doi.org/10.1021/acsnano.3c08233
ACS Nano 2023, 17, 22979−22989